Layer-Dependent Electronic Structure of Atomically Resolved Two-Dimensional Gallium Selenide Telluride

Amin Azizi,[†,‡] Gabriel Antonius,[†,§] Emma Regan,[†,∥,⊥] Rahmatollah Eskandari,[†] Salman Kahn,[†,∥] Feng Wang,[†,‡,∥] Steven G. Louie,[†,∥] and Alex Zettl*[,†,‡,∥]

[†]Department of Physics, University of California at Berkeley, Berkeley, California 94720, United States

[‡]Kavli Energy NanoScience Institute at the University of California, Berkeley, Berkeley, California 94720, United States

[§]Département de Chimie, Biochimie et Physique, Institut de recherche sur l'hydrogène, Université du Québec à Trois-Rivières, Trois-Rivières, Québec G8Z 4M3, Canada

[∥]Materials Sciences Division, Lawrence Berkeley National Laboratory, Berkeley, California 94720, United States

[⊥]Graduate Group in Applied Science and Technology, University of California at Berkeley, Berkeley, California 94720, United States

S Supporting Information

ABSTRACT: Alloying two-dimensional (2D) semiconductors provides a powerful method to tune their physical properties, especially those relevant to optoelectronic applications. However, as the crystal structure becomes more complex, it becomes increasingly difficult to accurately correlate response characteristics to detailed atomic structure. We investigate, via annular dark-field scanning transmission electron microscopy, electron energy loss spectroscopy, and second harmonic generation, the layered III−VI alloy $GaSe_{0.5}Te_{0.5}$ as a function of layer number. The local atomic structure and stacking sequence for different layers is explicitly determined. We complement the measurements with first-principles calculations of the total energy and electronic band structure of $GaSe_{0.5}Te_{0.5}$ for different crystal structures and layer number. The electronic band gap as well as the π and $\pi + \sigma$ plasmons are found to be sensitive to layer number.

KEYWORDS: *2D semiconductor alloys, $GaSe_{0.5}Te_{0.5}$, electronic structure, atomic structure, stacking order*
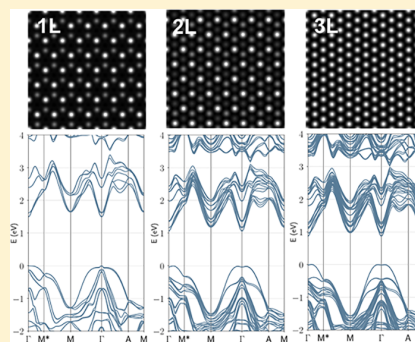
Among different two-dimensional (2D) material systems,[1−8] 2D semiconductor alloys[9−11] are highly adaptable systems where physical properties can be controlled not only by carrier doping, thickness, and strain but additionally by overall composition and structural phase tuning. Alloying and doping strategies have been developed for band-structure engineering of transition-metal dichalcogenides (TMDs) such as $MoS_{2(1−x)}Se_{2x}$[12,13] and $Mo_{1−x}W_xS_2$.[10,11,14] However, more complex alloy systems, where the constituent compounds have dissimilar structural phases, could be even more versatile due to potential structural phase engineering.

$M^{III}X^{VI}$ layered compounds (M = Ga, In; X = S, Se, Te) represent an important group of 2D compounds owing to their unique physical properties such as high carrier mobility, p-type behavior, and direct band gap for a variety of thicknesses.[15,16] Among them, bulk GaSe has a hexagonal crystal structure with a band gap of 2.1 eV,[17] whereas GaTe has a monoclinic structure with a band gap of 1.65 eV.[18] Fonseca et al. demonstrated the phase engineering of $GaSe_xTe_{1−x}$ alloys by showing that both hexagonal and monoclinic structures can be grown exclusively by controlling the composition.[19] It was found that the monoclinic structure is the stable structure when $x \leq 0.28$, while the hexagonal structure is the stable

phase when $x \geq 0.32$, and for x = 0.28−0.32 both phases coexist. Among different compositions of $M^{III}X^{VI}$ layered alloys, $GaSe_{0.5}Te_{0.5}$ and $GaS_{0.5}Te_{0.5}$ have intriguing potential for diverse applications, from photodetectors[20] to water-splitting catalysts.[21]

Although alloying can provide additional tunability of material properties, possible phase segregation in alloys due to immiscibility of constituent elements can hinder optimization. Determining the precise atomic arrangement of multispecies alloys is therefore of critical importance. However, as the number of atomic planes and atomic species in an alloy increases, it becomes increasingly challenging to determine the atomic structure and accurately correlate response characteristics to detailed atomic structure. Monolayer and bilayers of $GaSe_{0.5}Te_{0.5}$ alloys consist of 4 and 8 atomic-planes, respectively, in contrast to the relatively simple structures of graphene and h-BN (1 atomic-plane/monolayer) or even TMDs (3 atomic-planes/monolayer).

Here, we examine, experimentally and theoretically, the atomic-scale crystal structure and electronic band structure of
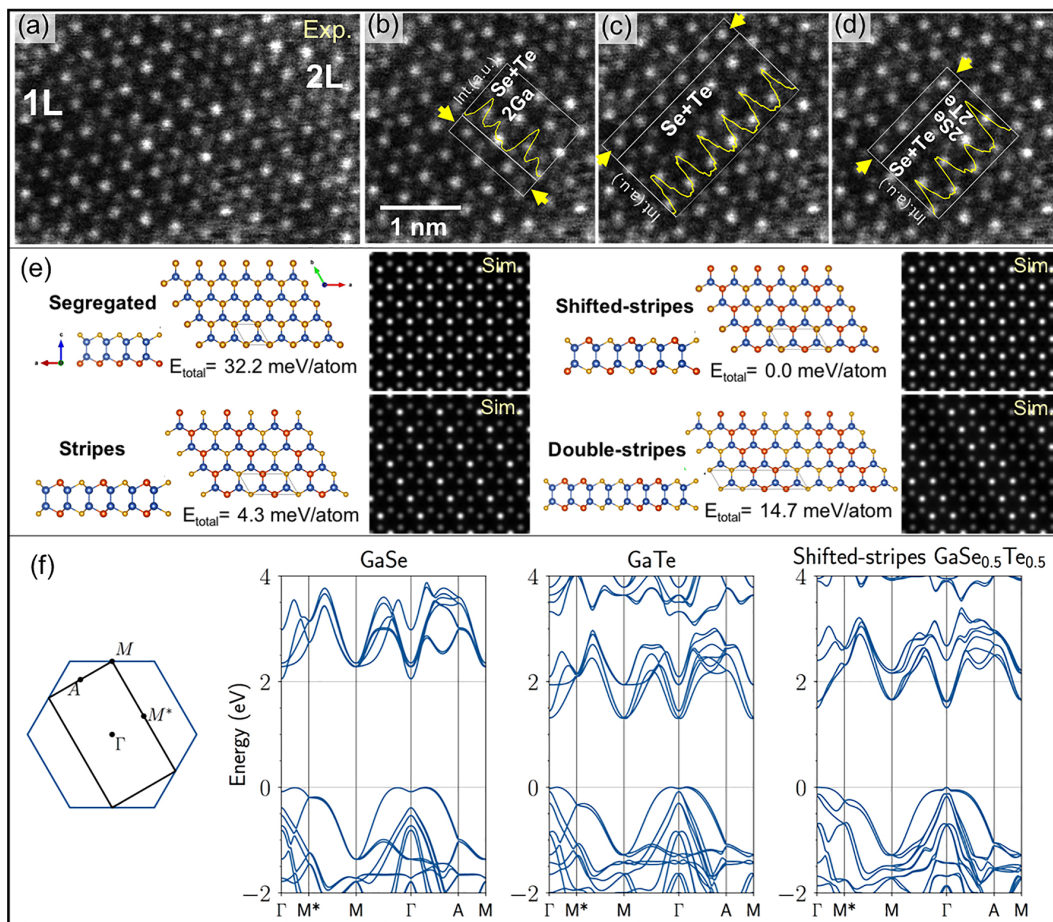
Figure 1. (a−d) Atomic-resolution ADF-STEM image of a monolayer $GaSe_{0.5}Te_{0.5}$ crystal and intensity line profiles for metal and chalcogen atomic columns along armchair and zigzag directions indicated by yellow arrows. (e) Side-view and top-view atomic models of four different possible geometries for the $GaSe_{0.5}Te_{0.5}$ monolayer and the corresponding simulated ADF-STEM image for each configuration. The DFT-PBE total energy of each configuration is taken relative to the lowest-energy structure. (f) The DFT-PBE Kohn−Sham band structure of the shifted-stripes $GaSe_{0.5}Te_{0.5}$ monolayer compared to that of the pure GaSe and GaTe monolayers.

$GaSe_{0.5}Te_{0.5}$ for different layer numbers. We employ annular dark-field scanning transmission electron microscopy (ADF-STEM) imaging and second harmonic generation (SHG). Owing to the Z-contrast mechanism in the ADF-STEM images, we directly map the position and chemical nature of different atomic species in a crystal and construct its atomic registry and stacking sequence. Using microscopic SHG measurements, we gain insight into the stacking of multilayer $GaSe_{0.5}Te_{0.5}$ with different crystal symmetry. In addition, we use low-loss electron energy loss spectroscopy (EELS) to probe changes in band gap and plasmons energy as a function of layer number. We complement our experiments with density functional theory (DFT) calculations that help to identify the stable crystal structure and corresponding electronic band structure.

Bulk $GaSe_{0.5}Te_{0.5}$ crystals are mechanically exfoliated and transferred onto TEM grids (see Methods in the Supporting Information). We use Z-contrast imaging in an aberration-corrected STEM to construct the atomic structure of the $GaSe_{0.5}Te_{0.5}$ ternary alloy to explore its compositional homogeneity. We investigate the atomic registries of monolayer, bilayer, and trilayer $GaSe_{0.5}Te_{0.5}$ and extract the corresponding atomic-scale crystal structure by comparing

atomic column intensity ratios in the ADF-STEM images combined with image simulations, DFT calculations, and SHG measurements.

Figure 1a shows an atomic-resolution ADF-STEM image of a monolayer $GaSe_{0.5}Te_{0.5}$ crystal next to a bilayer region. The monolayer shows a hexagonal structure with two distinct lattice sites with different intensities, i.e., brighter and dimmer spots (Figure 1a, b). Through analysis of the projected pattern, we find no phase segregation in the crystal, and the majority of chalcogen lattice sites show uniform intensities. For instance, the chalcogen atomic columns marked in Figure 1c have similar intensities, suggesting the presence of one Se and one Te in the chalcogen sites. Therefore, the brighter and dimmer spots in the ADF-STEM image correspond to the atomic columns with Se/Te atoms and 2Ga atoms, respectively (Figure 1b). A small number of chalcogen sites display ADF-STEM intensity higher or lower than the norm (Figure 1d), which suggests 2Se or 2Te instead of 1Se + 1Te. This is likely due to local fluctuations in the available chalcogen species during the growth.

To identify the distribution of the atoms within the monolayer $GaSe_{0.5}Te_{0.5}$, we compare four different possible geometries, as shown in Figure 1e. In the segregated structure
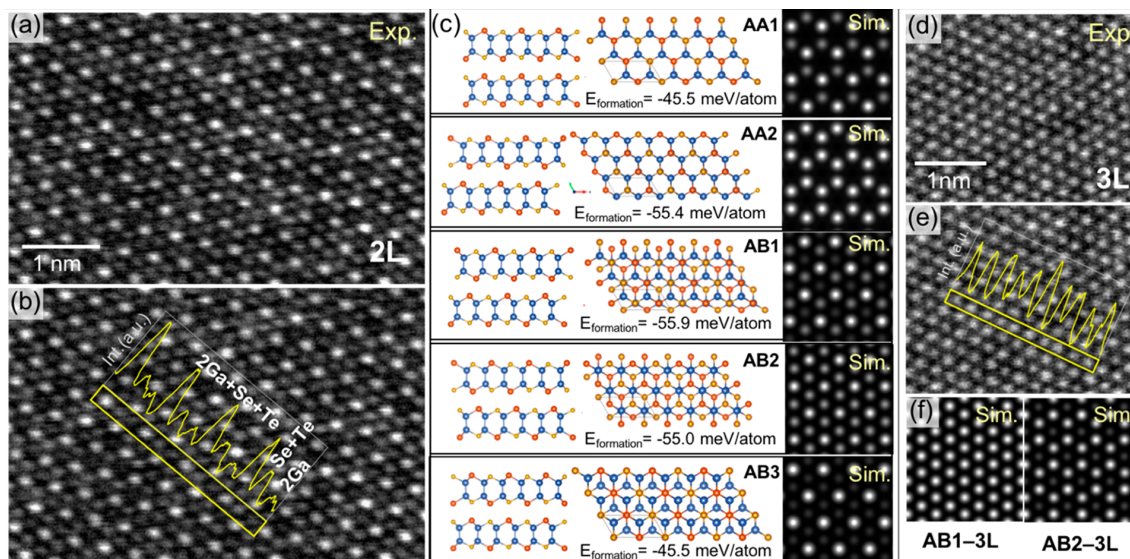
Figure 2. (a) ADF-STEM image of a bilayer $GaSe_{0.5}Te_{0.5}$ revealing its close-packed atomic structure with AB stacking and (b) the same data as in (a) with a line profile along the armchair direction (marked by yellow box), demonstrating three major distinct intensities for the atomic columns in the image. (c) Side-view and top-view schematics of five possible stacking geometries for the shifted-stripes bilayer and the corresponding simulated ADT-STEM images. (d) ADF-STEM image of a trilayer $GaSe_{0.5}Te_{0.5}$ and (e) the same data as in (d) with a line profile along the direction marked by yellow box, showing fairly uniform intensity for the atomic columns in the image. (f) Simulated ADF-STEM images of the trilayer $GaSe_{0.5}Te_{0.5}$ with AB1 (left) and AB2 (right) stacking.

(top left), the two chalcogen species (Se and Te) reside on opposite sides of the monolayer, and the unit cell contains a single unit formula of $GaSe_{0.5}Te_{0.5}$. In the stripes (lower left) and shifted-stripes (upper right) configurations, the chalcogens form chains of alternating species, and the unit cell contains two unit formula. In the stripes geometry, each chalcogen is facing the same species on the opposite side of the layer, while in the shifted-stripes geometry, they face a different species. In the double-stripes configuration (lower right), the chains of chalcogen species are doubled, and the unit cell contains four unit formula. By comparing the experimental ADF-STEM data to image simulations, we find that the monolayer $GaSe_{0.5}Te_{0.5}$ imaged in this work has either the segregated or shifted-stripes configuration, where the chalcogen lattice sites display a uniform intensity.

We perform DFT total energy calculations, using the PBE functional with van der Waals corrections[22] to help understand which atomic structure of monolayer $GaSe_{0.5}Te_{0.5}$ is most likely[23] (see Methods in the Supporting Information). The shifted-stripes, stripes, double-stripes, and segregated configurations have a total energy of 0, 4.3, 14.7, and 32.2 meV/atom, respectively. Hence, the shifted-stripes configuration has the lowest energy and is our preferred model. By adopting this model, we conclude that every gallium atom prefers to be coordinated with different chalcogen species (2Se + 1Te or 1Se + 2Te), and every chalcogen prefers to be facing a different chalcogen species.

Figure 1f shows the Kohn−Sham band structure of the shifted-stripes $GaSe_{0.5}Te_{0.5}$ monolayer, compared to that of the pure GaSe and GaTe monolayers. The Kohn−Sham band structures are computed at the DFT-PBE level, which underestimates the band gap by about 50% compared to previous GW calculations on these materials;[24] however, they provide accurate trends in comparing the salient features of the bands for the different atomic structures. For the pure GaSe

and GaTe systems, the last (doubly degenerate) occupied band, which has p_z-like character, features a caldera shape near Γ, and the band reaches its maximum along the $\Gamma-A$ (or $\Gamma-K$) direction. For $GaSe_{0.5}Te_{0.5}$, however, the second and third last (doubly degenerate) occupied bands, which have p_x- and p_y-like characters, pierce through the p_z-like valence band and become the highest occupied bands at Γ, giving the system a direct band gap. This behavior results from the breaking of the in-plane mirror symmetries in the shifted-stripes monolayer, allowing the valence bands to hybridize.

We turn now to bilayer $GaSe_{0.5}Te_{0.5}$. Figure 2a shows a Z-contrast ADF-STEM image of bilayer $GaSe_{0.5}Te_{0.5}$, which suggests a close-packed atomic structure with AB stacking. The selected intensity line-scan outlined in Figure 2b shows three distinct intensities for the atomic columns, representing 2Ga + 1Se + 1Te (the highest intensity), 1Se + 1Te (the second highest intensity), and 2Ga (the weakest intensity). Since bilayer $GaSe_{0.5}Te_{0.5}$ consists of 8 atomic planes and 3 atomic species, interpretation of the ADF-STEM image of Figure 2a is nontrivial. To aid in identification of the stacking sequence, we simulate ADF-STEM images of five possible stacking geometries for the shifted-stripes bilayer (Figure 2c), two configurations for AA stacking and three for AB stacking. The simulation for AB1 stacked bilayer $GaSe_{0.5}Te_{0.5}$ gives the best fit to the ADF-STEM data. We perform complementary DFT-PBE total energy calculations and determine the binding energy for the same five bilayer configurations presented above, with respect to two independent monolayers. The results are −55.9, −55.4, −55.0, −45.5, and −45.5 meV/atom for AB1, AA2, AB2, AA1, and AB3 configurations, respectively. The least stable geometries (AA1 and AB3) are the ones in which the chalcogens lie on top of one another. The other three geometries have similar binding energies and the AB1 stacking is the most stable one for bilayer $GaSe_{0.5}Te_{0.5}$, in agreement with our experimental ADF-STEM data. We also
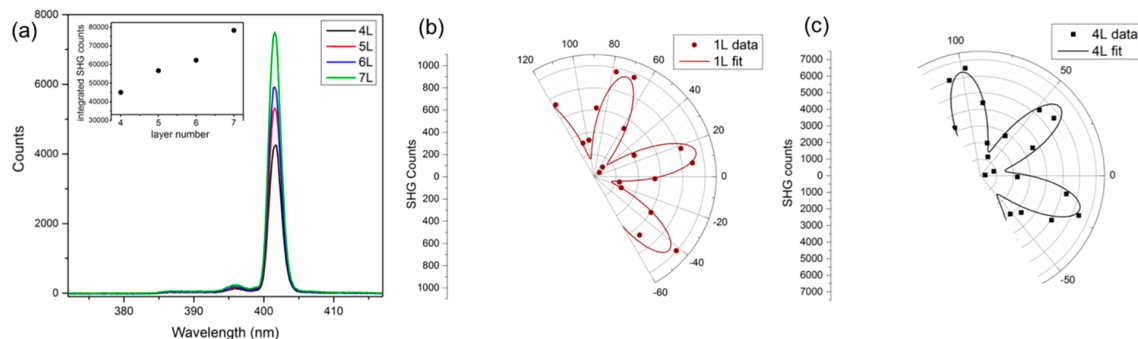
Figure 3. (a) Second harmonic generation from $GaSe_{0.5}Te_{0.5}$ crystals with different layer numbers, showing monotonically increasing SHG signal in 4−7 layer flakes. The inset demonstrates the integrated SHG counts for the flakes with different layer number. (b, c) The polarization-angle-dependent SHG intensity of monolayer and four-layer $GaSe_{0.5}Te_{0.5}$ crystals exhibiting a 6-fold rotational symmetry.
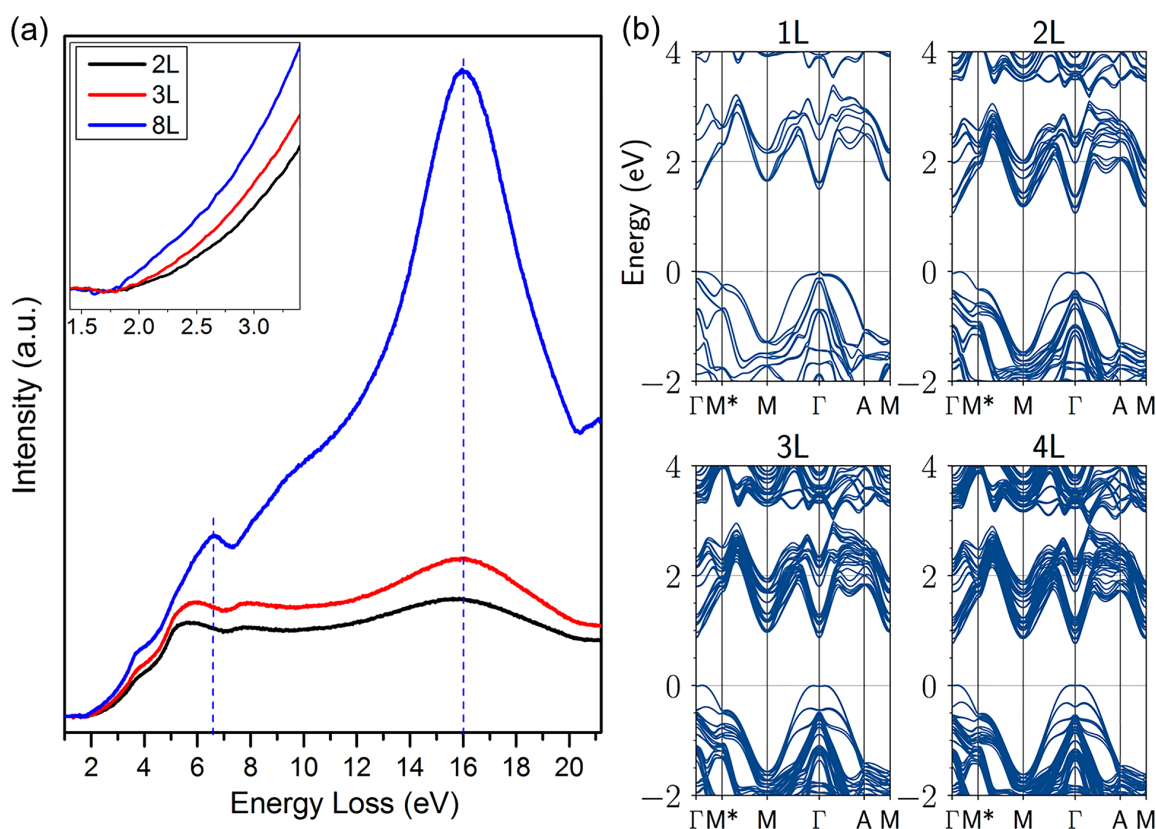

Figure 4. (a) Low-loss EELS spectra of 2L, 3L, and 8L samples. The inset shows a red shift in the onset of the EELS spectra as the layer number increases. (b) Evolution of the DFT-PBE Kohn−Sham band structure of $GaSe_{0.5}Te_{0.5}$ as the layer number increased from 1 to 4.

probed atomic structure of trilayer $GaSe_{0.5}Te_{0.5}$ to further help confirming the stacking of few-layer crystals (Figure 2d−e). Comparison of the experimental ADF-STEM image of trilayer $GaSe_{0.5}Te_{0.5}$ with the simulated images for the AB1 and AB2 stacking (Figure 2f) reveals that the AB1-stacked trilayer best resembles the observed atomic structure and agrees with our observation for the bilayer crystals.

Further insight into the stacking of multilayer $GaSe_{0.5}Te_{0.5}$ can be gained from microscopic SHG measurements. While noncentrosymmetric AB1 stacking in $GaSe_{0.5}Te_{0.5}$ should result in a SHG signal for any layer number, centrosymmetric AB2 stacking restores the inversion symmetry of the crystal

and should show negligible SHG intensity of even layers. A femtosecond laser at 800 nm is used to nonresonantly excite $GaSe_{0.5}Te_{0.5}$ flakes of 1−7 layers (see Figure S1 in the Supporting Information for the optical images of the flakes with different layer numbers). We observe SHG signal in all flakes, including those with an even number of layers. Figure 3a shows monotonically increasing SHG signal in 4−7 layer flakes. This is consistent with noncentrosymmetric AB1 stacking in $GaSe_{0.5}Te_{0.5}$. Strong SHG is also seen in thinner (1−3) layers, but the absolute counts are not reliable due to thin sample degradation over time. Furthermore, we probe the structural symmetry of the lattice using polarization-dependent

SHG measurements. We excite the sample with linearly polarized 800 nm light and detect the SHG intensity parallel to the excitation field. Both monolayer and four-layer SHG intensity display a 6-fold rotational symmetry as the polarization angle is varied, which is expected for a hexagonal crystal, in agreement with our ADF-STEM observations (Figure 3b, c).[25]

Due to low absorption of ultrathin GaSe, GaTe, and $GaSe_{0.5}Te_{0.5}$ crystals, there is some uncertainty in the band gap for these materials as a function of composition and thickness.[26] In agreement with previous studies,[26,27] we are unable to observe a photoluminescence (PL) peak in monolayer, bilayer, or few-layer $GaSe_{0.5}Te_{0.5}$ crystals. However, we do observe a PL peak at 1.76 eV for thick crystals (see Figure S2 in the Supporting Information), which is intermediate to the optical band-gaps reported for bulk GaSe[17] and GaTe.[18] To further probe the electronic structure in ultrathin crystals of $GaSe_{0.5}Te_{0.5}$, we perform low-loss EELS measurements. Figure 4a shows low-loss EELS spectra of bilayer (2L), trilayer (3L), and eight-layer (8L) crystals (see Figure S3 in the Supporting Information for the low-magnification ADF-STEM images of the 2L, 3L, and 8L flakes). The EELS spectra contain two main peaks at ~5.5−6.6 eV and ~15.8−16 eV, referred to as π and $\pi + \sigma$ plasmons. A red shift is observed for the π plasmon peak with increasing layer number. The $\pi + \sigma$ plasmon peak also slightly red shifts, while the peak intensity significantly increases for thicker samples. This observation of change in the plasmon peak energy and intensity in the EELS spectrum is analogous to what have been experimentally observed in TMDs[28] and graphene[29] and theoretically calculated for GaSe[30] and TMDs.[31] It has been attributed to the increased number of atoms and consequently number of bands, smaller volume per unit cell, and larger electron screening in thick samples (i.e., bulk) compared to monolayers.[31] In addition, we find that the onset of the EELS spectra red shift as the layer number increases, suggesting a decrease in the band gap from ~2.5 to ~2.2 eV. We also perform DFT calculations to study the evolution of the band structure as the number of $GaSe_{0.5}Te_{0.5}$ layers increased from 1 to 4 (Figure 4b). The last valence band is duplicated and recovers the caldera shape for 2 or more layers. As the layer number is increased, the depth of the caldera decreases, and the system evolves toward a direct band gap. At the same time, the band gap is reduced, in agreement with our experimental observation, thus enhancing the screening capabilities of the system.

In summary, we studied the $GaSe_{0.5}Te_{0.5}$ alloy and determined its detailed atomic structure using atomic-resolution ADF-STEM imaging, image simulations, SHG measurements, and DFT calculations. We found multilayer $GaSe_{0.5}Te_{0.5}$ crystals have a noncentrosymmetric AB stacking sequence. The EELS spectra show a steady decrease of the band gap with increasing numbers of layers, which is corroborated by DFT calculations. In addition, we identified that the energy of the π plasmon peak as well as the intensity of the $\pi + \sigma$ plasmon peak are largely affected by the layer number.

■ ASSOCIATED CONTENT

Ⓢ Supporting Information

The Supporting Information is available free of charge on the ACS Publications website at DOI: 10.1021/acs.nano-lett.8b04802.

Methods, optical images of the $GaSe_{0.5}Te_{0.5}$ flakes used for the SHG measurements, photoluminescence spectra of a thick $GaSe_{0.5}Te_{0.5}$ crystal, and low-magnification ADF-STEM image of $GaSe_{0.5}Te_{0.5}$ flakes used for the EELS measurements and the corresponding intensity profiles (PDF)

■ AUTHOR INFORMATION

Corresponding Author
*E-mail: azettl@berkeley.edu. Tel.: +1 (510) 642-4939. Fax: +1 (510) 642-2685.

ORCID Ⓘ
Amin Azizi: 0000-0001-9955-7228
Steven G. Louie: 0000-0003-0622-0170

Notes
The authors declare no competing financial interest.

■ REFERENCES

(1) Tan, C.; Cao, X.; Wu, X.-J.; He, Q.; Yang, J.; Zhang, X.; Chen, J.; Zhao, W.; Han, S.; Nam, G.-H.; Sindoro, M.; Zhang, H. *Chem. Rev.* **2017**, *117* (9), 6225−6331.
(2) Novoselov, K. S. *Science (Washington, DC, U. S.)* **2004**, *306* (5696), 666−669.
(3) Pacilé, D.; Meyer, J. C.; Girit, Ç. Ö.; Zettl, A. *Appl. Phys. Lett.* **2008**, *92* (13), 133107.
(4) Azizi, A.; AlSaud, M. A.; Alem, N. *J. Cryst. Growth* **2018**, *496−497*, 51−56.
(5) Mak, K. F.; Lee, C.; Hone, J.; Shan, J.; Heinz, T. F. *Phys. Rev. Lett.* **2010**, *105* (13), 136805.
(6) Azizi, A.; Zou, X.; Ercius, P.; Zhang, Z.; Elías, A. L.; Perea-López, N.; Stone, G.; Terrones, M.; Yakobson, B. I.; Alem, N. *Nat. Commun.* **2014**, *5* (1), 4867.
(7) Azizi, A.; Wang, Y.; Stone, G.; Elias, A. L.; Lin, Z.; Terrones, M.; Crespi, V. H.; Alem, N. *Nano Lett.* **2017**, *17* (5), 2802−2808.

(8) Azizi, A.; Eichfeld, S.; Geschwind, G.; Zhang, K.; Jiang, B.; Mukherjee, D.; Hossain, L.; Piasecki, A. F.; Kabius, B.; Robinson, J. A.; Alem, N. *ACS Nano* **2015**, *9* (5), 4882−4890.

(9) Huang, B.; Yoon, M.; Sumpter, B. G.; Wei, S.-H.; Liu, F. *Phys. Rev. Lett.* **2015**, *115* (12), 126806.

(10) Chen, Y.; Xi, J.; Dumcenco, D. O.; Liu, Z.; Suenaga, K.; Wang, D.; Shuai, Z.; Huang, Y.-S.; Xie, L. *ACS Nano* **2013**, *7* (5), 4610−4616.

(11) Azizi, A.; Wang, Y.; Lin, Z.; Wang, K.; Elias, A. L.; Terrones, M.; Crespi, V. H.; Alem, N. *Nano Lett.* **2016**, *16* (11), 6982−6987.

(12) Li, H.; Duan, X.; Wu, X.; Zhuang, X.; Zhou, H.; Zhang, Q.; Zhu, X.; Hu, W.; Ren, P.; Guo, P.; Ma, L.; Fan, X.; Wang, X.; Xu, J.; Pan, A.; Duan, X. *J. Am. Chem. Soc.* **2014**, *136* (10), 3756−3759.

(13) Mann, J.; Ma, Q.; Odenthal, P. M.; Isarraraz, M.; Le, D.; Preciado, E.; Barroso, D.; Yamaguchi, K.; von Son Palacio, G.; Nguyen, A.; Tran, T.; Wurch, M.; Nguyen, A.; Klee, V.; Bobek, S.; Sun, D.; Heinz, T. F.; Rahman, T. S.; Kawakami, R.; Bartels, L. *Adv. Mater.* **2014**, *26* (9), 1399−1404.

(14) Song, J.-G.; Ryu, G. H.; Lee, S. J.; Sim, S.; Lee, C. W.; Choi, T.; Jung, H.; Kim, Y.; Lee, Z.; Myoung, J.-M.; Dussarrat, C.; Lansalot-Matras, C.; Park, J.; Choi, H.; Kim, H. *Nat. Commun.* **2015**, *6*, 7817.

(15) Xu, K.; Yin, L.; Huang, Y.; Shifa, T. A.; Chu, J.; Wang, F.; Cheng, R.; Wang, Z.; He, J. *Nanoscale* **2016**, *8* (38), 16802−16818.

(16) Zhong, X.; Zhou, W.; Zhou, Y.; Zhou, F.; Liu, C.; Yin, Y.; Peng, Y.; Tang, D. *RSC Adv.* **2016**, *6* (65), 60862−60868.

(17) Rybkovskiy, D. V.; Arutyunyan, N. R.; Orekhov, A. S.; Gromchenko, I. A.; Vorobiev, I. V.; Osadchy, A. V.; Salaev, E. Y.; Baykara, T. K.; Allakhverdiev, K. R.; Obraztsova, E. D. *Phys. Rev. B: Condens. Matter Mater. Phys.* **2011**, *84* (8), 085314.

(18) Fonseca, J. J.; Tongay, S.; Topsakal, M.; Chew, A. R.; Lin, A. J.; Ko, C.; Luce, A. V.; Salleo, A.; Wu, J.; Dubon, O. D. *Adv. Mater.* **2016**, *28* (30), 6465−6470.

(19) Fonseca, J. J.; Horton, M. K.; Tom, K.; Yao, J.; Walukiewicz, W.; Dubon, O. D. *Chem. Mater.* **2018**, *30* (13), 4226−4232.

(20) Zhong, X.; Zhou, W.; Zhou, Y.; Zhou, F.; Liu, C.; Yin, Y.; Peng, Y.; Tang, D. *RSC Adv.* **2016**, *6* (65), 60862−60868.

(21) Bai, Y.; Zhang, Q.; Luo, G.; Bu, Y.; Zhu, L.; Fan, L.; Wang, B. *Phys. Chem. Chem. Phys.* **2017**, *19* (23), 15394−15402.

(22) Grimme, S.; Antony, J.; Ehrlich, S.; Krieg, H. *J. Chem. Phys.* **2010**, *132* (15), 154104.

(23) Gonze, X.; Jollet, F.; Abreu Araujo, F.; Adams, D.; Amadon, B.; Applencourt, T.; Audouze, C.; Beuken, J.-M.; Bieder, J.; Bokhanchuk, A.; Bousquet, E.; Bruneval, F.; Caliste, D.; Côté, M.; Dahm, F.; Da Pieve, F.; Delaveau, M.; Di Gennaro, M.; Dorado, B.; Espejo, C.; Geneste, G.; Genovese, L.; Gerossier, A.; Giantomassi, M.; Gillet, Y.; Hamann, D. R.; He, L.; Jomard, G.; Laflamme Janssen, J.; Le Roux, S.; Levitt, A.; Lherbier, A.; Liu, F.; Lukačević, I.; Martin, A.; Martins, C.; Oliveira, M. J. T.; Poncé, S.; Pouillon, Y.; Rangel, T.; Rignanese, G.-M.; Romero, A. H.; Rousseau, B.; Rubel, O.; Shukri, A. A.; Stankovski, M.; Torrent, M.; Van Setten, M. J.; Van Troeye, B.; Verstraete, M. J.; Waroquiers, D.; Wiktor, J.; Xu, B.; Zhou, A.; Zwanziger, J. W. *Comput. Phys. Commun.* **2016**, *205*, 106−131.

(24) Antonius, G.; Qiu, D. Y.; Louie, S. G. *Nano Lett.* **2018**, *18* (3), 1925−1929.

(25) Zhou, X.; Cheng, J.; Zhou, Y.; Cao, T.; Hong, H.; Liao, Z.; Wu, S.; Peng, H.; Liu, K.; Yu, D. *J. Am. Chem. Soc.* **2015**, *137* (25), 7994−7997.

(26) Cai, H.; Soignard, E.; Ataca, C.; Chen, B.; Ko, C.; Aoki, T.; Pant, A.; Meng, X.; Yang, S.; Grossman, J.; Ogletree, F. D.; Tongay, S. *Adv. Mater.* **2016**, *28* (34), 7375−7382.

(27) Pozo-Zamudio, O. D.; Schwarz, S.; Sich, M.; Akimov, I. A.; Bayer, M.; Schofield, R. C.; Chekhovich, E. A.; Robinson, B. J.; Kay, N. D.; Kolosov, O. V.; Dmitriev, A. I.; Lashkarev, G. V.; Borisenko, D. N.; Kolesnikov, N. N.; Tartakovskii, A. I. *2D Mater.* **2015**, *2* (3), 035010.

(28) Coleman, J. N.; Lotya, M.; O'Neill, A.; Bergin, S. D.; King, P. J.; Khan, U.; Young, K.; Gaucher, A.; De, S.; Smith, R. J.; Shvets, I. V.; Arora, S. K.; Stanton, G.; Kim, H.-Y.; Lee, K.; Kim, G. T.; Duesberg, G. S.; Hallam, T.; Boland, J. J.; Wang, J. J.; Donegan, J. F.; Grunlan, J. C.; Moriarty, G.; Shmeliov, A.; Nicholls, R. J.; Perkins, J. M.; Grieveson, E. M.; Theuwissen, K.; McComb, D. W.; Nellist, P. D.; Nicolosi, V. *Science (Washington, DC, U. S.)* **2011**, *331* (6017), 568−571.

(29) Eberlein, T.; Bangert, U.; Nair, R. R.; Jones, R.; Gass, M.; Bleloch, A. L.; Novoselov, K. S.; Geim, A.; Briddon, P. R. *Phys. Rev. B: Condens. Matter Mater. Phys.* **2008**, *77* (23), 233406.

(30) Ma, Y.; Dai, Y.; Guo, M.; Yu, L.; Huang, B. *Phys. Chem. Chem. Phys.* **2013**, *15* (19), 7098.

(31) Johari, P.; Shenoy, V. B. *ACS Nano* **2011**, *5* (7), 5903−5908.